NASA/TM—2010-216922

Modification of a Macromechanical Finite-Element Based Model for Impact Analysis of Triaxially-Braided Composites

Robert K. Goldberg
Glenn Research Center, Cleveland, Ohio

Brina J. Blinzler and Wieslaw K. Binienda
University of Akron, Akron, Ohio

December 2010

NASA STI Program . . . in Profile

Since its founding, NASA has been dedicated to the advancement of aeronautics and space science. The NASA Scientific and Technical Information (STI) program plays a key part in helping NASA maintain this important role.

The NASA STI Program operates under the auspices of the Agency Chief Information Officer. It collects, organizes, provides for archiving, and disseminates NASA's STI. The NASA STI program provides access to the NASA Aeronautics and Space Database and its public interface, the NASA Technical Reports Server, thus providing one of the largest collections of aeronautical and space science STI in the world. Results are published in both non-NASA channels and by NASA in the NASA STI Report Series, which includes the following report types:

- TECHNICAL PUBLICATION. Reports of completed research or a major significant phase of research that present the results of NASA programs and include extensive data or theoretical analysis. Includes compilations of significant scientific and technical data and information deemed to be of continuing reference value. NASA counterpart of peer-reviewed formal professional papers but has less stringent limitations on manuscript length and extent of graphic presentations.

- TECHNICAL MEMORANDUM. Scientific and technical findings that are preliminary or of specialized interest, e.g., quick release reports, working papers, and bibliographies that contain minimal annotation. Does not contain extensive analysis.

- CONTRACTOR REPORT. Scientific and technical findings by NASA-sponsored contractors and grantees.

- CONFERENCE PUBLICATION. Collected papers from scientific and technical conferences, symposia, seminars, or other meetings sponsored or cosponsored by NASA.

- SPECIAL PUBLICATION. Scientific, technical, or historical information from NASA programs, projects, and missions, often concerned with subjects having substantial public interest.

- TECHNICAL TRANSLATION. English-language translations of foreign scientific and technical material pertinent to NASA's mission.

Specialized services also include creating custom thesauri, building customized databases, organizing and publishing research results.

For more information about the NASA STI program, see the following:

- Access the NASA STI program home page at *http://www.sti.nasa.gov*

- E-mail your question via the Internet to *help@sti.nasa.gov*

- Fax your question to the NASA STI Help Desk at 443–757–5803

- Telephone the NASA STI Help Desk at 443–757–5802

- Write to:
  NASA Center for AeroSpace Information (CASI)
  7115 Standard Drive
  Hanover, MD 21076–1320

NASA/TM—2010-216922

Modification of a Macromechanical Finite-Element Based Model for Impact Analysis of Triaxially-Braided Composites

Robert K. Goldberg
Glenn Research Center, Cleveland, Ohio

Brina J. Blinzler and Wieslaw K. Binienda
University of Akron, Akron, Ohio

Prepared for the
25th Annual Technical Conference
cosponsored by the American Society for Composites (ASC) and the Japan Society for Composite Materials (JSCM)
Dayton, Ohio, September 20–22, 2010

National Aeronautics and
Space Administration

Glenn Research Center
Cleveland, Ohio 44135

December 2010

Level of Review: This material has been technically reviewed by technical management.

Available from

NASA Center for Aerospace Information
7115 Standard Drive
Hanover, MD 21076–1320

National Technical Information Service
5301 Shawnee Road
Alexandria, VA 22312

Available electronically at http://gltrs.grc.nasa.gov

Modification of a Macromechanical Finite-Element Based Model for Impact Analysis of Triaxially-Braided Composites

Robert K. Goldberg
National Aeronautics and Space Administration
Glenn Research Center
Cleveland, Ohio 44135

Brina J. Blinzler and Wieslaw K. Binienda
University of Akron
Akron, Ohio 44325

Abstract

A macro level finite element-based model has been developed to simulate the mechanical and impact response of triaxially-braided polymer matrix composites. In the analytical model, the triaxial braid architecture is simulated by using four parallel shell elements, each of which is modeled as a laminated composite. For the current analytical approach, each shell element is considered to be a smeared homogeneous material. The commercial transient dynamic finite element code LS-DYNA is used to conduct the simulations, and a continuum damage mechanics model internal to LS-DYNA is used as the material constitutive model. The constitutive model requires stiffness and strength properties of an equivalent unidirectional composite. Simplified micromechanics methods are used to determine the equivalent stiffness properties, and results from coupon level tests on the braided composite are utilized to back out the required strength properties. Simulations of quasi-static coupon tests of several representative braided composites are conducted to demonstrate the correlation of the model. Impact simulations of a represented braided composites are conducted to demonstrate the capability of the model to predict the penetration velocity and damage patterns obtained experimentally.

Introduction

The use of textile (woven and braided) polymer composites is being actively investigated for application in aerospace structures, as an alternative to metals or traditional laminated composites. For example, triaxially-braided composites are being utilized in fan cases for jet engines. To be certified as flight-worthy, a full-scale engine blade-out test must be performed to demonstrate that the fan containment system can contain a released fan blade and that the fan case can maintain sufficient structural integrity during the engine spool down. As part of the design process, the need exists to simulate the blade and case deformation, along with the resulting damage and failure, during a blade-out event through the use of commercial explicit finite element codes. For metallic case systems, a sufficient ability to properly simulate the blade-out event exists due to the fact that adequate material databases and engineering experience in correlating analysis and test results are available. However, the capability to simulate the impact response of composite materials is much less mature. The ultimate goal of the current research is to improve the blade-out simulation capability for composite fan cases to a level comparable to that available for metallic cases. The work presented in this paper is a step towards that goal.

There has been a significant amount of research conducted in the analysis and modeling of textile composites. The majority of the efforts have concentrated on various means to determine the effective mechanical properties of woven materials. Among the earliest attempts to model these materials was the work of Chou and Ishikawa (Ref. 1). In their original mosaic model, the woven composite was approximated as a one-dimensional series of laminated cross-ply composites, and classical laminate theory in combination with iso-stress or iso-strain assumptions were applied to obtain the effective stiffness properties of the material. They later extended the model to account for the fiber undulations that

are present in an actual woven material (Ref. 1). This approach was extended to two-dimensions by Naik and Shembekar (Ref. 2), where a mixture of parallel and series assumptions were applied to obtain the effective properties of the material. To analyze more complicated fiber architectures, such as braided composites, researchers such as Pastore and Gowayed (Ref. 3) and Byun (Ref. 4) modeled the fibers as a series of rods at various angles, and utilized simple iso-strain assumptions to obtain the overall effective properties of the composite. More sophisticated analysis methods, such as those developed by Tanov and Tabiei (Ref. 5) and Bednarcyk and Arnold (Ref. 6), used an approach where a representative unit cell of a woven composite was created, and then micromechanics-based approaches were applied to compute the effective properties and response of the material. In the context of applying these methods within a finite element model, elements are created with a homogenized set of material properties, and the appropriate analysis method is used to generate the effective properties and response of the woven material.

When many of these previously developed analytical methods have been used in combination with finite element analysis of a structure composed of woven or braided composite materials, homogenized elements are used, in which the architecture of the textile material is not directly accounted for within the finite element model. However, for triaxially-braided composites, experimental evidence has shown (Ref. 7) that when these materials are subject to impact, oftentimes the damage will propagate along the fiber directions. To best simulate these damage patterns, the braid architecture should be directly simulated within the finite element model. To account for the fiber architecture in a computationally efficient manner, Cheng (Ref. 8) created a "Braided Through the Thickness" approach, where the braided composite is modeled as a series of layered shell elements, where each element is a laminated composite with the appropriate fiber layup. The effective stiffness and strength material properties of the equivalent unidirectional composite then were included as input data for the finite element analysis. In the method developed by Cheng, fiber and matrix properties were combined using simple micromechanics-based approaches to obtain the required effective properties. The model was developed within the context of LS-DYNA (Ref. 9), a commercially available transient dynamic finite element code which is commonly used within the aerospace industry. A continuum damage mechanics-based composite constitutive model available within LS-DYNA was used as the material model.

Littell et al. (Ref. 10) made two major extensions to the approach developed by Cheng. First of all, in actual braided composites, the layers of braid often do not directly sit on top of each other, but instead fiber shifting takes place. In their work, the discretization of the braid was adjusted to account for this phenomenon. More significantly, in the previously developed methods, the effective unidirectional composite properties of the materials utilized in a braided composite either had to be measured experimentally or computed by using micromechanics techniques. This approach requires an extensive additional experimental program, with tests on either the matrix constituent (for micromechanics approaches) or the equivalent unidirectional composites, besides tests on the braided composite, being required to obtain the needed data. These test programs can be quite complicated, with no guarantee that the experimental properties obtained are representative of the in-situ properties of the material. In the approach developed by Littell, equivalent unidirectional properties were obtained from coupon tests of the braided composite. In this manner, the in-situ properties were directly incorporated into the input for the material model, which could reduce the amount of testing required. Also, this approach has the potential to accurately simulate the deformation, damage and failure of a triaxially-braided composite in a computationally efficient manner. Alternatively, an approach of this type can be useful as a tool to verify more sophisticated analysis approaches. As described by Littell, et al. (Ref. 10), the stiffness and strength values obtained through simulations of quasi-static coupon tests correlated reasonably well to experimentally obtained values. However, when flat panel impact tests were simulated, while the predicted penetration velocity correlated reasonably well with experimentally obtained values, the predicted damage patterns did not correlate well to what was observed experimentally.

In this paper, first the "Braided Through the Thickness" analysis method, and the differences between the approach utilized in this paper and the original methods developed by Cheng (Ref. 7) and Littell, et al. (Ref. 10) will be summarized and explained. Specifically, the original geometry as developed by Cheng (Ref. 7) (i.e., not accounting for the fiber shifting between layers) was utilized. However, as will be

described later in this paper, instead of utilizing a layered shell approach within each shell element to approximate the composite architecture, a semi-analytical approach was applied to determine the equivalent properties of each element based on the composite layup. The element itself was then modeled as a smeared continuum shell element. The philosophy developed by Littell, et al. (Ref. 10) of utilizing a "top-down" approach to determine the required strength properties for the material model is applied once again. However, the methodology was adjusted to reflect the different geometry of the analysis model and to account for the varying geometry within the composite unit cell in a more theoretically consistent manner. Simulations of quasi-static coupon tests and the correlation of the simulations to experimental results, for several representative composites will be described. Simulations of a flat panel impact test for a representative braided composite, and the comparison of the simulated penetration velocity and damage patterns to experimentally-obtained results will be described.

Overview of Analysis Approach

The "Braided Through the Thickness" analysis approach as developed by Cheng (Ref. 7) and Littell, et al. (Ref. 10) has currently been designed to analyze triaxially-braided polymer composites with a [0°/60°/–60°] braid architecture. In the braided composites, the 0° fibers have 24 k filaments per tow, while the 60° and –60° fibers have 12 k filaments per tow. Other triaxially-braided fiber architectures or theoretically any textile composite architecture can be analyzed using this approach. A unit cell of a typical triaxially-braided fiber preform is shown in Figure 1(a). In the figure, the ±60° bias fibers are visible on the surface. Portions of the 0° axial fibers that lie below the bias fibers can be seen in the open spaces between the bias fibers. An assumption in the methodology is that the fiber bundle spacing and number of fibers per fiber bundle are adjusted such that the fiber volume fractions in both the axial and bias directions are equal. In actuality, this particular fiber architecture is quasi-isotropic in-plane. Therefore the global in-plane stiffness should be the same in all directions, but this condition is not actually enforced within the context of the analysis model.

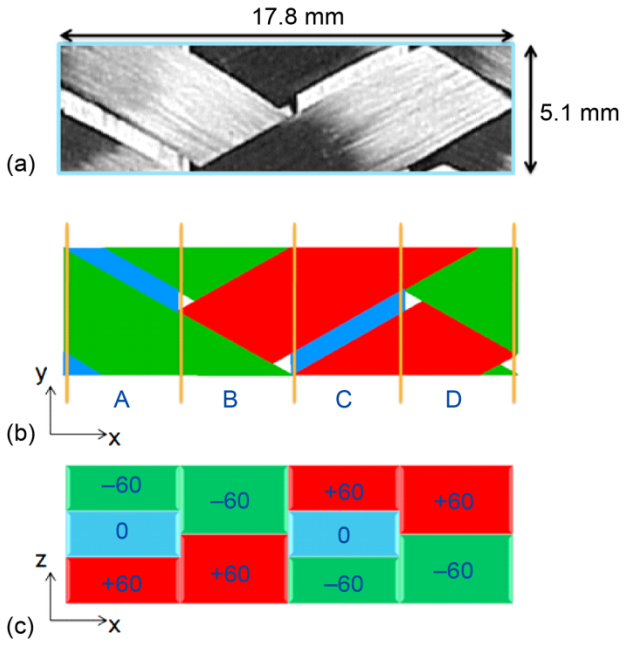

Figure 1.—Discretization of unit cell of triaxially-braided composite for braided through the thickness approach. (a) Digital image of unit cell. (b) Identification of axial and bias fibers within the unit cell. (c) Approximation of braid architecture of unit cell.

To apply the analysis approach, the braided-fiber architecture is idealized. As a first step in this process, a schematic of the top view of the fiber architecture is shown in Figure 1(b), where the –60° bias fibers are green, the 60° bias fibers are red, and the 0° axial fibers are blue. As shown in the figure, the unit cell can be divided into four equal length parallel subcells. Next, each subcell is approximated to be a laminated composite composed of a stack of fiber bundles at various orientations that are determined by the braid architecture. Subcell A is modeled as a [60°/0°/–60°] composite (bottom layer listed first). Subcell B is modeled as a [60°/–60°] composite, subcell C is modeled as a [–60°/0°/60°] composite, and subcell D is modeled as a [–60°/60°] composite. This idealization is shown in Figure 1(c). For subcells A and C, the fact that the 0° fiber tows have twice as many filaments per tow as the 60° and –60° layers is accounted for by making the 0° layer twice as thick as the remaining two layers. Each subcell can be modeled as an individual shell element in a finite element model. A unit cell then consists of four shell elements. Shell elements can be used since the length and width of the composite structures typically considered are much greater than the thickness. This conclusion can be justified based on impact tests discussed by Littell (Ref. 11), where the out-of-plane deformation in a flat panel impact test was found to be relatively small in relation to the panel dimensions. A full structure can then be modeled by replicating this four element unit cell throughout the finite element mesh. Each subcell is assumed to be equal thickness. In the one-layer model as described here, the plies in subcells B and D have lower overall fiber volume fractions due to the lack of axial fibers, resulting in these subcells only having two plies while subcells A and C have three plies. Note also that while each subcell is approximated as an anti-symmetric composite, the normal-bending coupling that is normally associated with a composite architecture of this type is assumed to be negligible. Due to the overall architecture of the braided composite, such coupling was not observed experimentally in composites of this type (Ref. 11). As a result, the portion of the laminate stiffness matrix (commonly referred to as the "B" matrix) that relates the in-plane loads to out-of-plane curvatures is assumed to be equal to zero. This approximation can be enforced due to the nature of the method used to model each subcell in the analysis model. Specifically, for this particular study, instead of modeling each subcell as a layered shell element, with each layer modeled explicitly within the finite element model (as was done by Cheng (Ref. 8) and Littell, et al. (Ref. 10)), each subcell was modeled as a smeared continuum shell element, with the effective stiffness properties determined using a combination of mechanics of materials-based micromechanics methods and classical laminate theory. The strength properties of each shell element are determined based on global coupon data from the braided composite. The details of how the stiffness and strength properties are determined will be described later in this paper. Applying a layered shell approach would allow for simulating the growth of damage in each layer independently, which could lead to an improved prediction of the damage patterns in the material due to impact. However, the approach of using smeared continuum shell elements for each subcell was chosen due to the fact that for the analyses in this paper difficulties were encountered in obtaining valid analytical results for a layered shell model using the applied constitutive model (to be discussed below). The assumption was made that even with using smeared continuum shell elements the overall damage patterns could be predicted adequately. Furthermore, another potential advantage of using smeared continuum elements for each subcell as opposed to a layered shell model would be an increase in computational efficiency. Computational efficiency is of key importance in simulating impact events on a full structure when the fiber tow dimensions are large enough that the composite architecture needs to be accounted for in the model.

The actual braided composites which were examined in this study had six layers of braided fibers (Fig. 2). For this study, a six layer model was created by stacking six of the single-layer models (Fig. 1(c)) on top of each other. The fiber shifting that sometimes occurs between layers, identified by Littell, et al. (Ref. 10), was not accounted for in this approach. By not accounting for the fiber shifting, and thus ensuring that the geometry of each subcell is different, the architecturally dependent damage that occurs during impact is more likely to be captured.

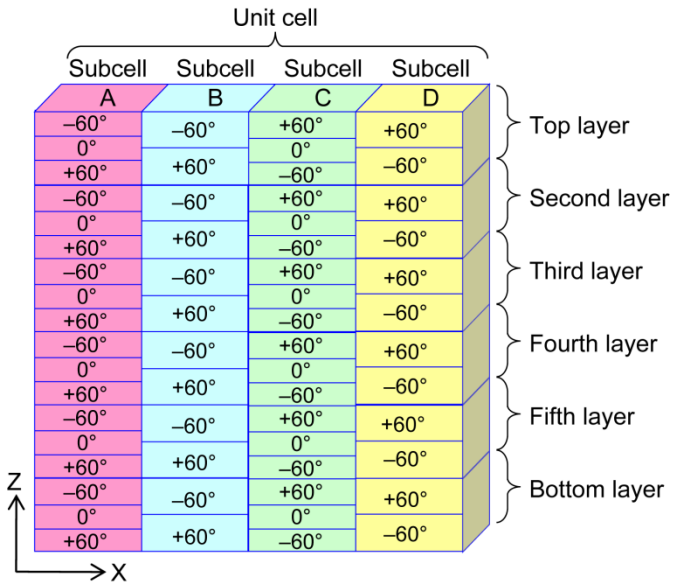

Figure 2.—Schematic of subcell discretization of six-layer triaxial braided composite.

Constitutive Model Overview

Due to the desire to apply this analysis methodology to the simulation of impact problems, the model was implemented within the context of LS-DYNA (Ref. 9), a commercially available transient dynamic explicit finite element code that is widely used within the aerospace industry to conduct impact analyses. The constitutive model resident within LS-DYNA that was chosen for use with the analysis method is a continuum damage mechanics-based model for unidirectional composites, based on a theory developed by Matzenmiller, et al. (Ref. 12), that is implemented in LS–DYNA as MAT_58. The failure criterion implemented in the model is based on the Hashin failure criterion. For this material model, the required input stiffness parameters include the unidirectional-ply-level (or material axis system-based) axial and transverse modulus, in-plane shear modulus, and the in-plane Poisson's ratio. The unidirectional-ply-level (or material axis system-based) strength data that is required includes the axial tensile and axial compressive failure stress and failure strain, the transverse tensile and transverse compressive failure stress and failure strain, and the in-plane shear failure stress and failure strain. The stiffness values are used by the material model to simulate the initial linear portion of the composite response. The ply-level strength and ultimate strain values are used to determine the nonlinear portion of the material response and to determine how the damage parameters used as internal variables within the material model evolve over the loading cycle. Furthermore, the user may specify a "stress-limiting factor" in the longitudinal and/or transverse directions. If the value of the "stress-limiting factor" is set to zero, the failure stress value is assumed to occur at the specified failure strain, and the material model then "connects the dots" (including enforcing any required material nonlinearity) in order to create the best-fit stress strain curve that accounts for the specified stiffness and strength values. If the "stress limiting factor" is set to one, the stress-strain curve of the composite is assumed to increase linearly until the maximum strength value is reached. At that point, the material is assumed to act as if it were a perfectly plastic material, with the strain in the specified direction increasing with no increase in stress until such point as the specified strain level is reached, at which point material failure is assumed to occur. These ideas are shown schematically in Figure 3.

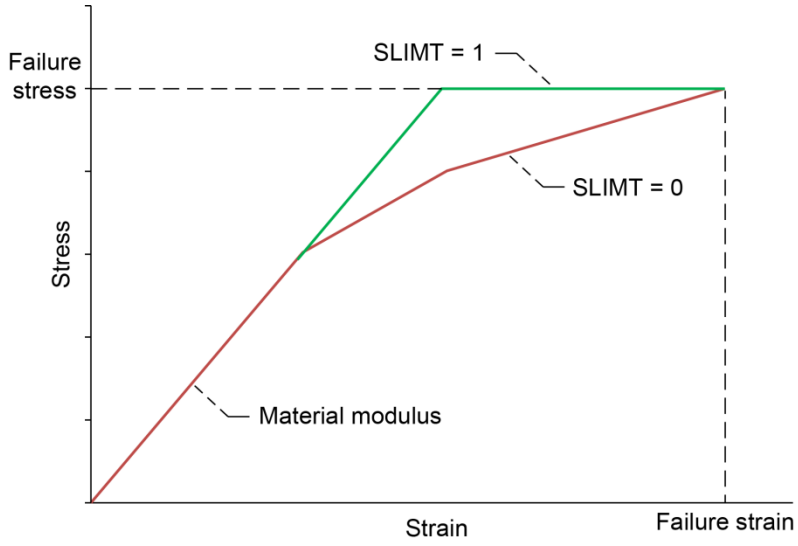

Figure 3.—Schematic showing effect of “stress-limiting parameter.”

For this study, since each subcell was modeled as a smeared homogeneous continuum, the properties that were input for the constitutive model were the effective stiffness and strength properties for each subcell, not the properties of the individual composite layers represented within the subcell. For each element, the longitudinal material direction was assumed to be along the axial (0°) fibers, and the in-plane transverse material direction was assumed to be perpendicular to this direction. Therefore, the composite unit cell was approximated as four orthotropic subcells (one element per subcell) joined together. The constitutive behavior of each subcell was simulated using the above-described material model. Two sets of material properties were required to analyze the unit cell. Subcells A and C required one set of stiffness and strength properties, since they represented a composite with 0°, 60°, and –60° layers. Since the composites were balanced, even though the location of the 60° and –60° layers were different for subcells A and C, the effective stiffness and strength properties were assumed to be the same. In a similar manner, stiffness and strength properties had to be defined for subcells B and D. Again, since these two subcells both represented a composite with a 60° layer and a –60° layer, the properties of both subcells were assumed to be the same. Note that the properties of subcells A and B were different not only because of the different fiber layups, but due to the fact that the local fiber volume fractions of the two subcells were different due to the presence or lack of axial fibers and pure matrix pockets in the subcell (Fig. 1(b)).

The properties required by the model described above are the properties of the subcell, which is treated as an effective orthotropic material. A fundamental problem in the analysis of textile composites is that the representative lamina properties are not known and cannot be directly measured. Attempts can be made to fabricate unidirectional laminates using the same fiber tows that are used to make the preform. This approach is often not easy to accomplish, and the properties of the unidirectional lamina could be different from the properties of the fiber tows within the textile composite because of processing differences. For these reasons, a method was chosen that utilizes an approach based on a combination of classical laminate theory and concepts from composite micromechanics theory to calculate the lamina stiffness properties using a “bottom-up” approach, where the constituent properties were homogenized through the use of micromechanics theory to obtain the effective ply level properties, and then classical laminate theory was applied to obtain the effective stiffness properties of the subcell. To determine the strength properties for each subcell, properties from experimental data obtained on the braided composite were applied using a “top-down” approach to determine the required parameters. The details on this methodology will be discussed later in this paper. Although there are also some limitations in using this approach to determine the strength properties, the experimental requirements are simplified, and the calculated lamina properties represent the in-situ properties of each subcell within the braided composite.

Determination of Material Properties

A computer program was developed to compute the effective stiffness and strength properties for each subcell based on the input of the fiber volume ratio of each subcell, fiber and matrix constitutive properties, and failure stress and failure strain data for the braided composite obtained through coupon level tests. Details of the procedures incorporated into the program are given below.

Stiffness Properties

Determining the stiffness properties to input into the constitutive model is a two-step procedure. First, given the fiber and matrix stiffness properties as listed in Littell (Refs. 10 and 11) and the subcell fiber volume ratio, micromechanics methods were used to determine the effective unidirectional stiffness properties of a single ply of the composite in the subcell. For this study, a micromechanics method developed by Sun and Chen (Ref. 13) was utilized due to the combination of accuracy of the method combined with the availability of simple analytical expressions to determine the effective stiffness properties. This combination was deemed beneficial in terms of utilizing the procedures in the context of a standalone program. The input data required by the micromechanics method includes the fiber volume ratio, the longitudinal, transverse, and shear fiber modulus, the fiber Poisson's ratio, and the matrix modulus and Poisson's ratio. For the micromechanical calculations, the average fiber volume ratio for each subcell was determined based on high fidelity finite element models of triaxially-braided composites developed by Li, et al. (Ref. 14), which were generated based on detailed measurements of representative braided composite geometries. From the finite element models, volumes corresponding to the equivalent subcell volumes in the "Braided Through the Thickness" simplified model were identified. The equivalent average fiber volume ratio in the selected volumes (corresponding to the subcells) was then calculated numerically from the mesh of the high-fidelity finite element model, based on the volume of fiber tows, local fiber volume fraction of the fiber tows (identified in Li, et al. (Ref. 14)), and the volume of any pure resin regions present in the identified volume. For the composites analyzed in this study, subcells A and C were found to have an average fiber volume ratio of 0.65, and subcells B and D were found to have an average fiber volume ratio of 0.50.

Once the unidirectional stiffness properties for each subcell were computed, classical laminate theory (Ref. 15) was applied to obtain the overall effective stiffness for the subcell. For this study, only in-plane loads were assumed to be applied, which resulted in the moment curvature relations of classical laminate theory being neglected. In-plane normal-shear couplings were absent since the subcells were approximated as balanced laminates. Furthermore, as discussed earlier, even though the composite layups were anti-symmetric, tension-bending coupling was neglected. For purposes of computation, the composites were assumed to have unit thickness, so the loads per unit length could be approximated as stresses. The above assumptions were applied to write the constitutive equation for each subcell, such as is shown below for subcell A

$$\begin{pmatrix} \sigma_{11}^{A} \\ \sigma_{22}^{A} \\ \sigma_{12}^{A} \end{pmatrix} = \begin{bmatrix} A_{11}^{A} & A_{12}^{A} & 0 \\ A_{12}^{A} & A_{22}^{A} & 0 \\ 0 & 0 & A_{66}^{A} \end{bmatrix} \begin{pmatrix} \varepsilon_{11}^{A} \\ \varepsilon_{22}^{A} \\ \gamma_{12}^{A} \end{pmatrix} \tag{1}$$

where A_{ij}^{A} represents the stiffness matrix components for subcell A, σ_{ij}^{A} represents the stresses in subcell A, ε_{ij}^{A} represents the normal strains in subcell A and γ_{ij}^{A} represents the engineering shear strains in subcell A. In this and all following equations, the "11" direction is assumed to be along the 0° fibers, the "22" direction is assumed to be perpendicular to the 0° fibers in the plane of the composite, and the "12" direction is assumed to be the in-plane shear direction. The stiffness matrix components were computed using the usual procedures of classical laminate theory (Ref. 15). Specifically, the unidirectional stiffness

matrix for a single ply of each subcell was computed based on the computed effective engineering properties. Next, the A matrix terms are written in terms of Q-bar, the transformed stiffness terms for a unidirectional ply in the structural axis system and the ratio of the ply thickness to the overall thickness in the manner of classical laminate theory as follows

$$A_{ij} = \sum_{k} \bar{Q}_{ij} * t_k \tag{2}$$

where the sum is taken over the layers k, and t_k is the thickness ratio of the k^{th} layer. For subcell A, the expansion can be written as follows

$$\begin{aligned} A_{11}^{A} &= \bar{Q}_{11}^{60\,\text{deg}} * t + \bar{Q}_{11}^{0\,\text{deg}} * 2t + \bar{Q}_{11}^{-60\,\text{deg}} * t \\ A_{12}^{A} &= \bar{Q}_{12}^{60\,\text{deg}} * t + \bar{Q}_{12}^{0\,\text{deg}} * 2t + \bar{Q}_{12}^{-60\,\text{deg}} * t \\ A_{22}^{A} &= \bar{Q}_{22}^{60\,\text{deg}} * t + \bar{Q}_{22}^{0\,\text{deg}} * 2t + \bar{Q}_{22}^{-60\,\text{deg}} * t \end{aligned} \tag{3}$$

and in a similar manner the expansion for subcell B can be written. Note that for subcells A and C the thickness ratio of the 0° (axial) layer was taken to be 0.5 and the thickness ratio of the 60° and –60° (bias) layers were taken to be 0.25. This is due to the fact that the axial fiber tows for the composites used in this study were composed of 24 k flattened tows and the bias fiber tows were composed of 12 k flattened tows, leading to the axial fiber tows having a greater number of fibers. This fact is reflected in the "2*t*" terms in the "A" matrix calculations relating to the 0° layers. For subcells B and D, due to the lack of axial fibers the thickness ratio for both the 60° and –60° (bias) layers was taken to be 0.50. Based on the computed stiffness matrix terms, the required engineering constants for each subcell could then be determined using the usual procedures of orthotropic elasticity theory (Ref. 15).

Strength Properties

To compute the strength properties for each subcell required by the LS-DYNA MAT_58 constitutive model (Ref. 9), data obtained from global axial tension and compression (loading along the direction of the axial fibers), transverse tension and compression (loading perpendicular to the direction of the axial fibers), and in-plane shear coupon level tests were utilized. Note that for the constitutive model that is utilized for this study both the stresses and strains in the various component directions at failure are required to be input. As shown in Figure 3, the failure stresses and strains are used along with the "stress-limiting parameter" to construct the appropriate stress-strain response for the composite. Particularly in simulating an impact event, where the stresses are highly multiaxial, properly determining all of the strength parameters is critical. The key step in the algorithm was utilizing a mechanics of materials approach to specify what the stresses and strains in each subcell were given an applied global stress. In this way, global failure stresses and strains were related to the local stresses and strains in the individual subcells at points of failure. These local stresses and strains were then utilized as the failure stresses and strains in the subcell for the MAT_58 constitutive model. Referring back to the subcell architecture as defined in Figures 1(b) and (c), and assuming each subcell had equal width (equal to 0.25 of the total width of the composite), the following iso-stress and iso-strain assumptions, referred to as the mechanics of materials assumptions (Ref. 15) were defined

$$
\begin{aligned}
&\varepsilon_{11}^{A} = \varepsilon_{11}^{B} = \varepsilon_{11}^{C} = \varepsilon_{11}^{D} = \varepsilon_{11} \\
&0.25\varepsilon_{22}^{A} + 0.25\varepsilon_{22}^{B} + 0.25\varepsilon_{22}^{C} + 0.25\varepsilon_{22}^{D} = \varepsilon_{22} \\
&0.25\gamma_{12}^{A} + 0.25\gamma_{12}^{B} + 0.25\gamma_{12}^{C} + 0.25\gamma_{12}^{D} = \gamma_{12} \\
&0.25\sigma_{11}^{A} + 0.25\sigma_{11}^{B} + 0.25\sigma_{11}^{C} + 0.25\sigma_{11}^{D} = \sigma_{11} \\
&\sigma_{22}^{A} = \sigma_{22}^{B} = \sigma_{22}^{C} = \sigma_{22}^{D} = \sigma_{22} \\
&\sigma_{12}^{A} = \sigma_{12}^{B} = \sigma_{12}^{C} = \sigma_{12}^{D} = \sigma_{12}
\end{aligned}
\tag{4}
$$

where stress and strain values without superscripts represent the global stress and strain values, and superscripted values represent the stresses and strains in the particular subcell. Note that due to the assumptions of the analysis approach, the stresses and strains in subcells A and C are equal, as are the stresses and strains in subcells B and D. As will be described below, for different types of loading the expressions in Equation (4) were manipulated and combined with the stiffness matrix equations for each subcell to relate the failure stresses and strains for each subcell to the global failure stresses and strains observed for the composite.

To compute the axial tension failure stress and failure strain for each subcell, data obtained from axial tension tests on the braided composite were utilized. Representative results from an axial tension test on a T700S/E-862 triaxially-braided composite obtained by Littell (Ref. 11) (to be described in more detail later in this paper) are shown in Figure 4. As can be seen in the figure, the axial tension stress-strain curve became nonlinear at a stress level of approximately 495 MPa, and failed at a stress level of approximately 800 MPa. To relate the global stresses to subcell stresses, Equation (4) was combined with the subcell stiffness matrix equations. For the special case of axial tension loading, all of the stresses except the longitudinal tension stress (σ_{11}) were set equal to zero. As shown in Equation (4), due to the simplified nature of the discretization of the unit cell the transverse and shear stresses in each subcell are assumed to

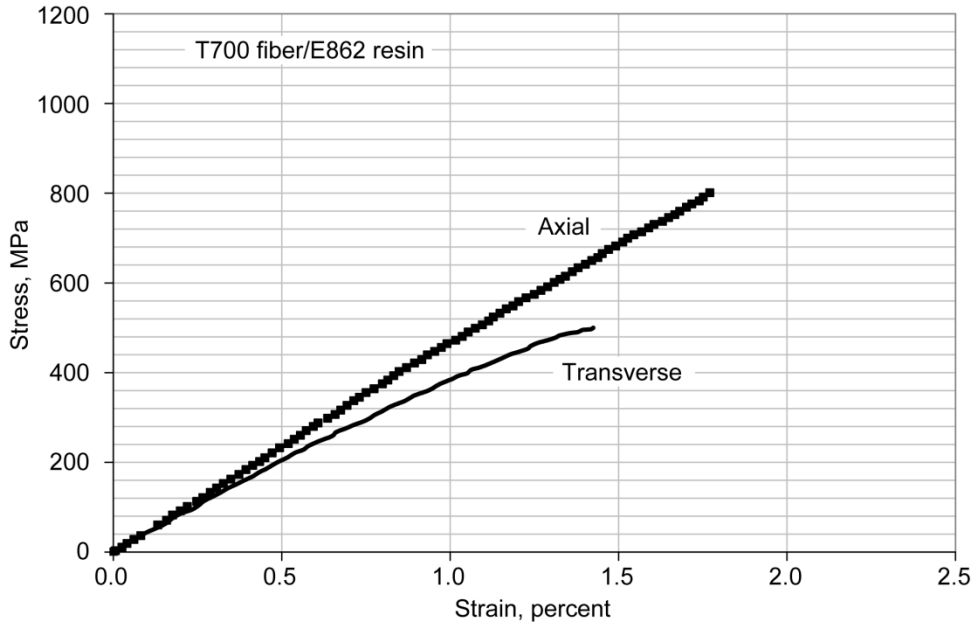

Figure 4.—Axial and transverse tensile material response curves for T700 fiber/E862 resin material system.

be equal and equal to the global stress. For the case of uniaxial tensile loading, the global applied transverse and shear stresses are equal to zero. The following expressions relating the stresses in subcells A and B to the global applied longitudinal tension stress were obtained as follows:

$$\sigma_{11}^{B} = \frac{\sigma_{11}}{0.5\left(1+\frac{S_{11}^{B}}{S_{11}^{A}}\right)}, \sigma_{11}^{A} = \frac{S_{11}^{B}}{S_{11}^{A}}\sigma_{11}^{B} \tag{5}$$

where S_{11} is the "11" component of the compliance matrix (inverse of the stiffness matrix) for the appropriate subcell (A or B). Since the ultimate failure in an axial tension test of a triaxially-braided composite has been found to be primarily due to the failure of the axial fibers (Ref. 10), the axial failure stress for subcell A (and by extension subcell C) (which has axial fibers) was determined using Equation (5) with the ultimate composite failure stress being utilized as the global applied stress. The axial failure stress for subcell B (and by extension subcell D) was computed using the global stress level at which the axial tension stress-strain curve became nonlinear. The rationale for making this assumption was based on observations made by Littell (Ref. 11) on the local response of braided composites during an axial tension test. During the course of an axial tension test, large strains in the bias fiber tows in the direction perpendicular to the load were observed by using digital image correlation methods to view full-field surface strains, indicating that local matrix microcracking within the bias fiber tows leading to bias fiber tow failure (at least in the transverse direction) occurred well before the ultimate strength of the composite was reached. In addition, local delaminations were observed to take place in the bias fiber tows during axial loading. For this study, the assumption was made that the effects of these bias fiber tow failures would be most pronounced in subcells B and D since no axial fibers were present in those subcells. Furthermore, the assumption was made that the stress level at which these local failures in the bias fiber tows occurred (or at least became significant) was at least loosely correlated to the stress level at which the global stress-strain curve became nonlinear. These assumptions are justified based on observations made by Littell (Ref. 11). For composites where the bias fiber tow failure was not as pronounced and initiated at higher stress levels, the stress level at which the global axial tension stress-strain curve became nonlinear was much higher. Furthermore, the global stress level at which the stress-strain curve became nonlinear was at least loosely correlated to the stress level at which fiber splitting and out-of-plane delaminations occurred (Ref. 11). Therefore, as mentioned above, the local axial stress in subcell B (and subcell D) at the global stress level where the axial tension stress-strain curve became nonlinear was used as the failure stress for the subcell. Even though on a local level the bias fiber failure occurred in the transverse fiber direction, due to the large fiber angle of the bias fibers on the global homogeneous subcell level the effects were most pronounced in the global axial direction. Since the failure stresses for subcells B and D were much lower than the failure stresses for subcells A and C, the "stress-limiting parameter" was set to one (1) for subcells B and D. In this manner, once the failure stress in these subcells was reached, the stress would be held at a constant level, but strain could accumulate until the ultimate failure strain was reached. This behavior is displayed schematically in Figure 3. By applying this approach, premature failure of the simulations (since the composite could still accumulate strain even after the bias fibers failed) would be avoided and the analysis would be consistent with the approximations applied in the theory. To determine the axial failure strain for each subcell, which is also required for the constitutive model, based on the uniform strain assumptions shown in Equation (4), the axial tension failure strain for all of the subcells was set equal to the global axial tension failure strain of the composite.

To compute the axial compression failure stress and failure strain for each subcell, data obtained from axial compression tests on the braided composite were utilized. Representative results from an axial compression test on a T700S/E-862 triaxially-braided composite obtained by Littell (Ref. 11) (to be described in more detail later in this paper) are shown in Figure 5. For the case of axial compression,

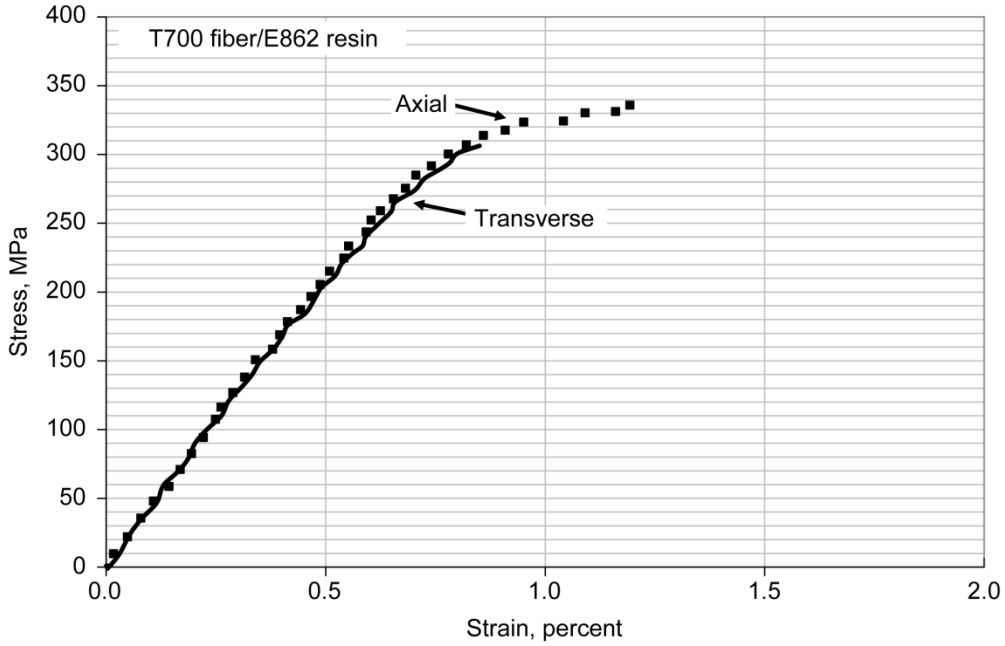

Figure 5.—Axial and transverse compressive material response curves for T700 fiber/E862 resin material system.

detailed examination of full-field strain data obtained during the tests by Littell (Ref. 11) indicated that the strain field was nearly uniform throughout the gage section, indicating that no local fiber tow damage was occurring before the final failure of the composite. Therefore, all of the subcells were assumed to fail simultaneously when the global axial compression-failure stress was reached. To compute the local axial compression-failure stress in each subcell, the global axial compression stress was used in Equation (5) to compute the local subcell stresses. Even though the stress-strain curve shown in Figure 5 is nonlinear and the expressions in Equation (5) are based on a linear elastic response, the assumption was made that the ratio of the local subcell stresses to the global applied stress remained constant. To remain consistent with the approximations of the theory, the axial compression-failure strain for each subcell was set equal to the global axial compression-failure strain. With the specification of the initial modulus, failure stress and failure strain of each subcell, the MAT_58 constitutive model used for the analysis was then capable of enforcing the required nonlinearities in the material response.

To compute the transverse tension-failure stress and-failure strain for each subcell, data obtained from transverse tension tests on the braided composite (along with data from the axial tension tests for reasons to be described below) were utilized. Representative results from a transverse tension test on a T700S/ E-862 triaxially-braided composite obtained by Littell (Ref. 11) (to be described in more detail later in this paper) are shown in Figure 4. As can be seen in the figure, while the initial stiffness of the axial and transverse curves are the same, the transverse tension results become nonlinear at a much lower stress as compared to the axial tension results and the material fails at a much lower stress in transverse tension as compared to axial tension. Theoretically, since the triaxially-braided composites are nominally quasi-isotropic, the axial tension- and transverse tension-failure stresses should be much closer to each other. The reasons for this discrepancy were discussed in detail by Littell, et al. (Refs. 10 and 11). As discussed in these papers, premature failure near fiber bundles that terminate at free edges can influence the shape of the stress-strain curve and the measured failure strain. A large amount of edge damage was observed in both axial and transverse tensile tests. In an axial tensile test the axial braid fibers lie along the specimen axis and are gripped on both ends during a test. Since these axial braid fibers carry most of the load, the reduction in strength caused by edge damage is small for the axial tensile test. The edge damage has a larger effect on the measured strength for the transverse tensile test because all of the axial braid fibers are

perpendicular to the applied load. There is no continuous load path between the grips through fibers because all axial and bias fiber bundles terminate at a free edge. The edge damage contributes to the nonlinearity of the experimental transverse-tensile stress-strain curve and also contributes to the reduced transverse-failure stress compared with the axial failure stress. Full-field strain measurements during the transverse tensile tests revealed regions of low strain up to 10 percent of the specimen width that were not carrying load because of edge damage. Since the damaged region did not carry load, the stress in the undamaged region was about 10 percent higher than the stress that was calculated based on the initial cross-sectional area of the specimen. The experimental transverse stress-strain curve was therefore not an accurate representation of the transverse tensile properties.

Due to the fact that the transverse tensile results obtained experimentally were not accurate indications of the actual behavior of the material under transverse tensile loading conditions, indirect methods were utilized to obtain the transverse tensile failure stress and failure strain for each subcell. As a first approximation, the global transverse tension failure stress was assumed to be equal to the global axial-tension failure stress. For a quasi-isotropic material, this approximation theoretically should be valid and anecdotal evidence (Refs. 10 and 11) indicates that in actual structures the transverse tensile strength should be very close to the axial tensile strength. Following the approximations specified in Equation (4), the transverse tensile-failure stress in each subcell was set equal to the global axial-tension failure stress. To relate the global transverse stress to the subcell strains, Equation (4) was combined with the subcell constitutive equations. The following expressions relating the strains in subcells A and B to the global applied transverse-tension stress were obtained as follows:

$$\varepsilon_{22}^{A} = S_{12}^{A}\left(\frac{S_{12}^{B} - S_{12}^{A}}{S_{11}^{A} + S_{11}^{B}}\right)\sigma_{22} + S_{22}^{A}\sigma_{22}$$
$$\varepsilon_{22}^{B} = S_{12}^{B}\left(\frac{S_{12}^{A} - S_{12}^{B}}{S_{11}^{A} + S_{11}^{B}}\right)\sigma_{22} + S_{22}^{B}\sigma_{22} \tag{6}$$

where S_{ij} is the "ij" component of the compliance matrix (inverse of the stiffness matrix) for the appropriate subcell (A or B). To apply Equation (6) to compute the transverse tensile failure strain for each subcell, a phenomenon that was discovered by Littell, et al. (Refs. 10 and 11) was incorporated into the algorithm. During the transverse tensile tests, large strains in the transverse direction in the axial fiber tows were observed, indicating that local matrix microcracking within the axial fiber tows leading to axial fiber tow failure (at least in the transverse direction) occurred well before the ultimate strength of the composite was reached. These results indicated that the behavior of subcells A and C in the transverse direction likely resembled an "elastic-plastic" response, where before the "fiber splitting" occurred the transverse stiffness was equal to the initial elastic value, but once "fiber splitting" occurred the subcells could accumulate strain but not stress, and the local modulus was reduced to a very small value. Therefore, at the point of transverse-tensile failure the overall transverse stiffness of subcells A and C was most likely not equal to the initial elastic stiffness value, but instead was reduced due to the transverse failure in the axial fiber tows. As a first approximation to account for this effect, when Equation (6) was applied in the property calculation algorithm the transverse compliance matrix value for subcell A ($S_{22}{}^{A}$) was doubled from the initial elastic value to reflect the reduced stiffness due to the local microcracking in the axial fiber tows.

To compute the transverse compression-failure stress and failure strain for each subcell, data obtained from transverse compression tests on the braided composite were utilized. Representative results from a transverse compression test on a T700S/E-862 triaxially braided composite obtained by Littell (Ref. 11) (to be described in more detail later in this paper) are shown in Figure 5. For the case of transverse compression, similar to the case for axial compression, detailed examination of full-field strain data obtained during the tests by Littell (Ref. 11) indicated that the strain field was uniform throughout the gage section,

indicating that no local fiber tow damage was occurring before the final failure of the composite. Therefore, all of the subcells were assumed to fail simultaneously when the global transverse compression-failure stress was reached. To compute the local transverse compression-failure stress in each subcell, once again the assumptions given in Equation (4) were applied and the subcell failure stresses were assumed to be equal to the global composite transverse compression-failure stress. To compute the subcell transverse compression-failure strains, an expression similar to Equation (6) was used with some modifications. First, Equation (6) was used directly with the global transverse compression-failure stress as input. However, the strains computed using Equation (6) could not be utilized directly due to the fact that, as observed in Figure 5, the transverse compression response of the composite is nonlinear, and Equation (6) was developed assuming a linear elastic response. Next, the ratio of each subcell strain to the total transverse compression strain under elastic conditions (computed using the second expression in Equation (4)) was determined. The assumption was then made that the strain ratio under elastic conditions was identical to the actual strain ratio. Therefore, the strain ratio for each subcell was scaled using the actual transverse compression-failure strain to obtain the transverse compression failure strain for each subcell.

To compute the in-plane shear failure stress and failure strain for each subcell, a procedure very similar to that utilized for the case of transverse compression was utilized. Once again, detailed examination of full-field strain data obtained during coupon level tests by Littell (Ref. 11) indicated that the strain field was uniform throughout the gage section, indicating that no local fiber tow damage was occurring before the final failure of the composite. Therefore, all of the subcells were assumed to fail simultaneously when the global in-plane shear failure stress was reached. To compute the local in-plane shear failure stress in each subcell, once again the assumptions given in Equation (4) were applied and the subcell failure stresses were assumed to be equal to the global composite in-plane shear failure stress. To compute the subcell in-plane shear-failure strains, Equation (6) was used with some modifications. First, Equation (6) was used directly with the in-plane shear failure stress as input. However, the strains computed using Equation (6) could not be utilized directly due to the fact that, while not shown here, the in-plane shear response of the composite is nonlinear, and Equation (6) was developed assuming a linear elastic response. Next, the ratio of each subcell strain to the total in-plane shear strain under elastic conditions was determined. The assumption was then made that the strain ratio under elastic conditions was identical to the actual strain ratio. Therefore, the strain ratio for each subcell was scaled using the actual in-plane shear-failure strain to obtain the in-plane shear-failure strain for each subcell.

Simulation of Quasi-Static Tension Tests

A series of simulations was conducted to evaluate the analysis methods described above. Specifically, quasi-static axial and transverse coupon-level tensile tests on two representative triaxially-braided composites were simulated. At this time, only the tensile response was simulated due to the relative simplicity of the finite element models. In the future, to fully evaluate the material model compressive and shear tests will also be simulated. The materials were composed of a two-dimensional triaxial-braided preform and a 177 °C (350 °F) cure epoxy resin. For both materials, TORAYCA T700S fibers (Toray Carbon Fibers America, Inc.), a high strength, standard modulus carbon fiber was used. For the first material, EPICOTE Resin 862/EPIKURE Curing Agent W system (Hexion Specialty Chemicals) (E-862 for short), a two-part low viscosity system was used. For the second material, CYCOM PR 520 (Cytec Industries, Inc.), a one part toughened resin, was used.

A [0°/60°/–60°] triaxial-braid architecture was manufactured. The 0° axial fibers were 24 k flattened tows while the ±60° bias fibers were 12 k flattened tows. Although larger fiber bundles were used in the axial direction, the fiber bundle spacing in the axial and bias directions were adjusted to give the same fiber volume in the axial and bias directions. This is a nominally quasi-isotropic in-plane fiber architecture, so the global in-plane stiffness is expected to be the same in all directions when the region of

interest includes several unit cells of the braid material. Composite panels were fabricated by placing six layers of the braided preform into a mold with the 0° fibers aligned in the same direction. Although the axial (0°) fibers in the various layers were aligned, the lateral position of the axial tows in the six layers was random. Resin was injected into the closed mold and cured according to processing conditions recommended by the resin manufacturer. The global fiber-volume ratio of the cured composites was measured using the acid digestion technique. Both the T700S/PR520 and T700S/E-862 composites had a global fiber volume of 55.9±0.18 percent.

The finite element meshes used in the study are shown in Figure 6. The finite element model for the axial tension test was 30.48 cm (12.0 in.) long and 3.56 cm (1.40 in.) wide and had 369 nodes and 320 shell elements. The model for the transverse tensile test was 30.48 cm (12 in.) long and 3.56 cm (1.40 in.) wide and had 522 nodes and 476 elements. The fixed end of the model was constrained in all three displacement and rotation directions. The loading was displacement-controlled at the rate of 0.0635 cm/s (0.025 in./s), which was consistent with the test conditions. Each subcell was modeled as a shell element, which allowed the braid architecture to be explicitly modeled with the finite element mesh of the coupon. In Figure 6, the red elements represent subcell A, the blue elements represent subcell B, the green elements represent subcell C, and the yellow elements represent subcell D. The unit cell orientations for both of the modeling conditions are highlighted in Figure 6 for reference. In the axial test simulation, the unit cell is oriented parallel to the direction of the applied load. In the transverse test simulation, the unit cell is oriented perpendicular to the direction of the applied load. While not discussed in this report, the entire specimen was modeled as opposed to a single unit cell in order to investigate the ability of the method to simulate the damage patterns that occur during a coupon test.

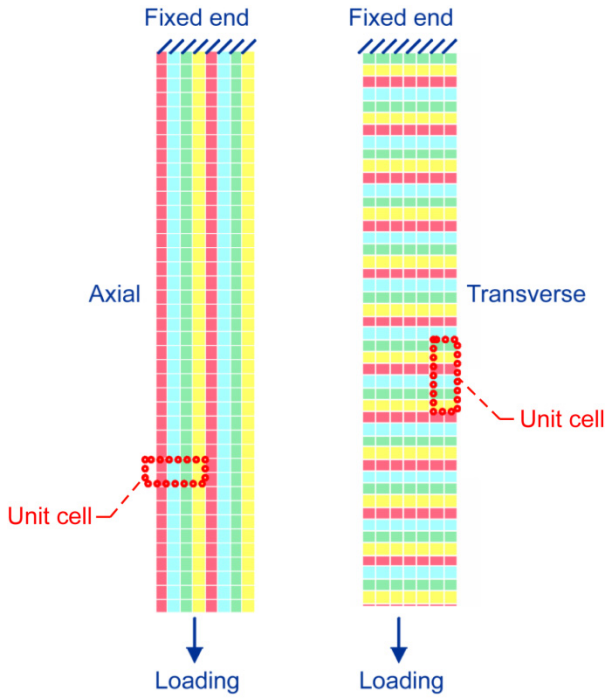

Figure 6.—Finite element models of axial tension (left) and transverse tension (right) tests.

To compute the stiffness properties for each subcell, first the subcell fiber volume ratios were determined as discussed earlier. In applying the micromechanics analysis methods, the stiffness properties for the fiber and matrix given in Table 1 were applied. Given the observations made by Littell (Ref. 11) that the measured stiffness properties for both of the braided composites were approximately the same, identical stiffness properties for both of the resin systems were used (based on values listed by Littell (Ref. 11) for the PR520 resin). The equivalent stiffness properties (along with the equivalent strength properties) for each subcell for each of the two material systems are given in Table 2. To determine the equivalent strength properties for each subcell, the methods and procedures discussed in the previous section were applied. The numerical values of the global failure stresses and failure strains that were utilized to compute the equivalent subcell strength properties for each of the two materials are given in Table 3. The equivalent strength values that were computed for each of the two materials are given in Table 2.

TABLE 1.—CONSTITUENT PROPERTIES

	E_{11} (GPa)	E_{22} (GPa)	ν_{12}	G_{12} (GPa)
T700 (Fiber)	230.00	15.00	0.20	27.00
E-862 (Resin)	4.00	4.00	0.36	1.47
PR520 (Resin)	4.00	4.00	0.36	1.47

TABLE 2.—MATERIAL PROPERTY VALUES USED FOR THE QUASI-STATIC COUPON SIMULATIONS

Material	T700–E862		T700–PR520	
Material Parameter Name (LS-DYNA name)	(MPa)		(MPa)	
Subcell	A&C	B&D	A&C	B&D
Axial modulus (EA)	80815	8111	80815	8111
Transverse modulus (EB)	47215	37536	47215	37536
In plane shear modulus (GAB)	14982	23041	14982	23041
In plane Poisson ratio (PRBA)	0.175	1.464	0.175	1.464
Axial tensile failure strain (E11T)	0.018	0.018	0.024	0.024
Axial compressive failure strain (E11C)	0.012	0.012	0.019	0.019
Transverse tensile failure strain (E22T)	0.035	0.013	0.045	0.017
Transverse compressive failure strain (E22C)	0.009	0.007	0.014	0.010
In plane shear failure strain (GMS)	0.024	0.016	0.029	0.019
Axial tensile stress at failure (XT)	1454	90	1905	191
Axial compressive stress at failure (XC)	613	62	687	69
Transverse tensile stress at failure (YT)	800	800	1048	1048
Transverse compressive stress at failure (YC)	305	305	346	346
In plane shear stress at failure (SC)	257	257	308	308
Stress limiting parameter for axial tension (SLIMT1)	0	1	0	1
Stress limiting parameter for transverse tension (SLIMT2)	0	0	0	0
Stress limiting parameter for axial compression (SLIMC1)	0	0	0	0
Stress limiting parameter for transverse compression (SLIMC2)	0	0	0	0
Stress limiting parameter for shear (SLIMS)	0	0	0	0

TABLE 3.—GLOBAL STRESS VALUES USED IN CALCULATIONS

(MPa)	T700/E862	T700/PR520
Global stress at failure (Axial tension)	800	1048
Global stress at failure (Transverse tension)	800	1048
Global stress at failure (Axial compression)	337	378
Global stress at failure (Transverse compression)	305	346
Global stress at failure (Shear)	257	308
Stress at pt. of nonlinearity (Axial tension)	495	1048
Global strain at failure (Axial compression)	0.012	0.019
Global strain at failure (Transverse compression)	0.008	0.012
Global strain at failure (Shear)	0.020	0.024

Tensile stress versus strain curves were generated for both the T700S/E-862 and T700S/PR520 materials in the axial and transverse directions to examine the correlation of the analysis model to the test data. Even though the coupon level test data was used to obtain the input data applied to the model, due to the complexity of the material model and the ways that the various stiffness and strength parameters interact, the stiffnesses and strengths predicted by the analytical simulations may not necessarily correspond to the parameters determined from the test data. Specimen failure was deemed to occur when all of the elements in a row failed. The element failure occurred nearly simultaneously in the simulations, leading to a fairly abrupt ultimate failure. The resulting stress-strain curves for the E-862 system are shown in Figure 7 (axial tension) and Figure 8 (transverse tension). The resulting stress-strain curves for the PR520 system are shown in Figure 9 (axial tension) and Figure 10 (transverse tension). In these figures the test data is as determined by Littell, et al. (Ref. 10).

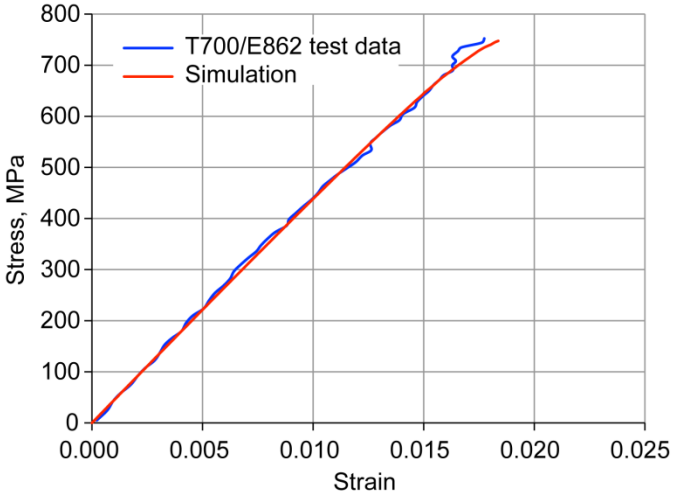

Figure 7.—Axial tension experimental versus computed stress/strain response for T700/E862 composite coupon test.

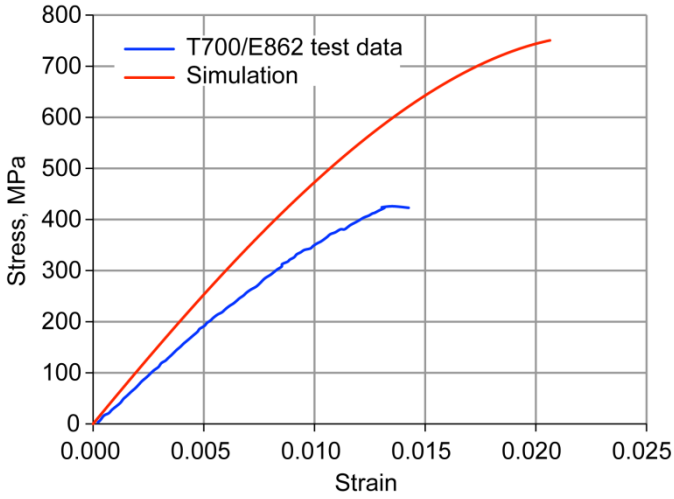

Figure 8.—Transverse tension experimental versus computed stress/strain response for T700/E862 composite coupon test.

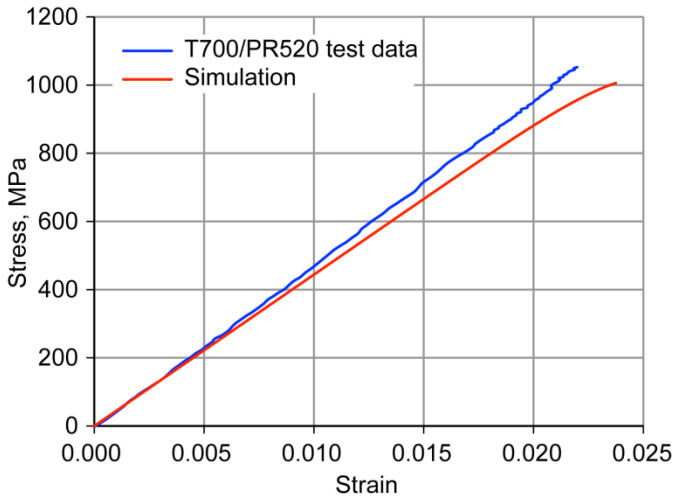

Figure 9.—Axial tension experimental versus computed stress/strain response for T700/PR520 composite coupon test.

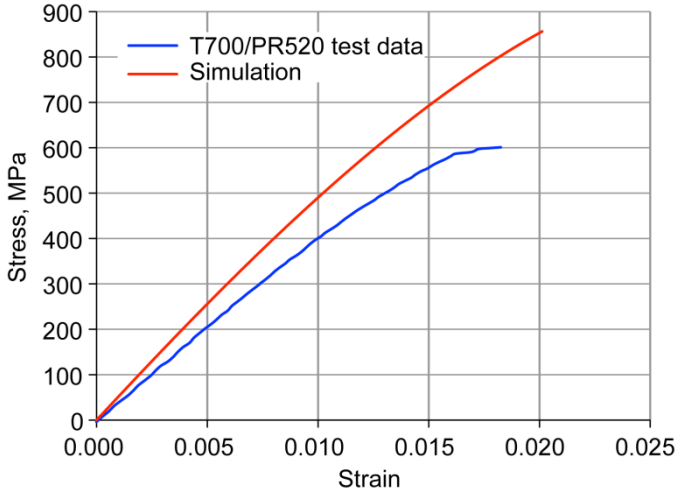

Figure 10.—Transverse tension experimental versus computed stress/strain response for T700/PR520 composite coupon test.

For the axial tension test, for both materials the deformation response and ultimate failure stress computed by the simulations correlated well with the experimental results. The initial stiffness was well correlated for both materials. The nonlinearity in the stress-strain curve for the E-862 material was correlated well. The simulation of the axial tension response of the PR520 material displayed some nonlinearity that was not present in the experimental response, but the maximum error was approximately 7 percent. The reasons for this discrepancy are unclear and need to be explored further. The ultimate strength of the transverse tensile specimen was significantly overpredicted, and the simulated response of the transverse tensile test was much more linear than observed in the experiments for both materials. As mentioned earlier, the most likely cause of the discrepancy in the transverse tensile results is due to the edge damage and low strain zones that were observed in the experimental transverse-tension tests, leading to the experimental transverse stress-strain curve not being an accurate representation of the true composite tensile response. Due to the way in which the braid architecture was discretized and simulated in the analytical model, with the fiber tows not being modeled in a continuous manner, these local effects could not be captured in the simulations as each subcell in a sense is an independent laminated composite. As a result, the simulated results from the transverse tension test in all likelihood were more

representative of the response that would be observed if the response was measured at a location far away from where edge effects would be significant. Therefore, the fact that the simulated transverse-tension response of the material was more linear than the experimental results, with a transverse-failure stress only slightly lower than the axial-failure stress, was consistent with the strength properties input into the constitutive model (with the assumptions discussed above) and most likely actually more representative of the response of the material as utilized in an engineering structure. In a qualitative sense, the simulated transverse tension results are consistent with the expected response of the material, but a full detailed quantitative examination of the transverse tension simulation results will only be possible when improved experimental results are obtained.

Simulation of Impact Tests

The composite materials presented in this research are sometimes used in impact situations. This section presents preliminary investigations which use the developed composite models for impact simulations for the detection and prediction of impact velocity thresholds and failure depictions. The T700/E862 material system was examined for the impact simulations.

In the impact tests, which were conducted in the NASA Glenn Research Center Ballistic Impact Laboratory and which are described in detail in Reference 16, a single stage compressed-gas gun was used to propel an aluminum 2024 projectile into 30.5 cm (12 in.) by 30.5 cm (12 in.) by 3.2 mm (0.125 in.) composite panels. The composite panel was held in a circular fixture with an aperture of 20.54 cm (10 in.). The projectile was a thin-walled hollow AL 2024 cylinder with a nominal mass of 50 gm and a front face with a compound radius. The overall length of the projectile was 4.95 cm (1.947 in.), the wall thickness was 0.076 cm (0.030 in.), and the nominal diameter was 5.067 cm (1.995 in.). Tests were performed over a range of impact velocities to determine the velocity for onset of damage, the growth of damage with increasing velocities, the penetration threshold, and the damage pattern induced by penetration. Twelve panel tests were conducted using impact velocities ranging from 157 m/s (515 ft/s) to 175 m/s (573 ft/s). The threshold velocity for penetration was between 161 m/s (530 ft/s) and 168 m/s (550 ft/s).

To conduct simulations of the impact tests described above, the flat panels used in the impact tests were modeled using a finite element mesh 0.3048 m (12 in.) wide, 0.3048 m (12 in.) tall and 0.3175 cm (0.125 in.) thick with 2700 shell elements. The finite element model of the panel, including the circular boundary conditions that were applied to simulate the experimental conditions, is shown in Figure 11. The simulated panels had a clamped boundary in a 25.4 cm (10 in.) diameter circle at the center. The

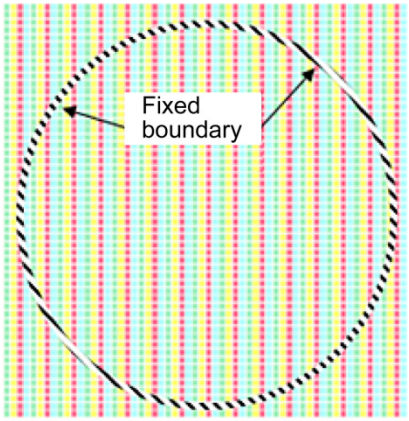

Figure 11.—Finite element mesh for impact simulations.

nodes in this boundary had all six degrees-of-freedom constrained. The panel was made up of 810 unit cells; 15 unit cells across and 54 unit cells vertically. The alternating patterns of pink, blue, green, and yellow represent the four subcells of the unit cell used to simulate the composite braid geometry. The projectile was modeled as a linear elastic material to accurately account for energy absorption due to elastic deformation of the projectile. The density and stiffness of the projectile in the simulation were measured from the aluminum used in the experimental tests (Ref. 16). The contact algorithm that used was the LS-DYNA contact "Contact_Automatic_Single_Surface," (Ref. 9).

Simulations were run for various impact velocities above and below the penetration threshold. The penetration threshold in the simulations was defined as the velocity at which the projectile fully penetrated the plate with a residual projectile velocity of zero. The model predicted penetration taking place at an impact velocity of 160 m/s (525 ft/s), which was only slightly below the experimental threshold velocity of 161 to 168 m/s (530 to 550 ft/s). The reason for the slight discrepancy could be related to the fact that quasi-static properties were utilized to compute the equivalent strength parameters applied in the analysis. The actual response and properties of the material may be a function of strain rate, with the various failure stresses and strains being higher at higher strain rates. Future efforts will investigate the effects on the predictions of using strain rate-dependent material properties.

A photograph of the damage patterns that were obtained in a panel impacted near the threshold velocity is shown in Figure 12, with a diagram of the simulated impact damage patterns shown next to it. The unsymmetric damage patterns observed in the simulation results was due to the fact that the projectile rotated during the simulations and did not impact exactly head on. The projectile rotation has also been observed in the experimental tests (Ref. 16). In the experimental impact test failure initiated along the axial fibers in the center of the specimen and then propagated outward along both the axial and the bias fibers. The simulated results predicted a similar damage pattern with the failure initiating along the bias fibers around the edges of the damage area, then propagating horizontally, and finally zipping vertically near the center of the damage area. However, in the simulation, a more rounded opening than that seen in the experimental tests was created. It is possible this difference could be due again to the use of quasi-static properties. There may be some anisotropic stiffening due to rate effects. Further research will be done to investigate the effects of strain rate.

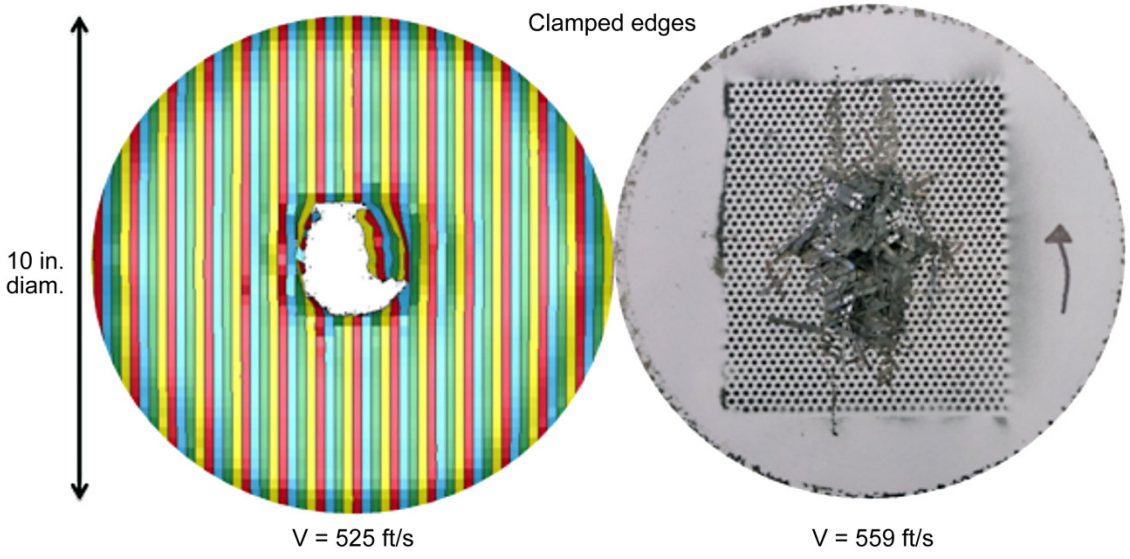

Figure 12.—Simulated (left) and experimental (right) damage patterns for T700/E862 composite subjected to impact.

Conclusions

A macro-level finite element-based approach has been developed which allows for the simulation of the response of a triaxially-braided composite in a manner which takes into account the architecture of the braided material within a structure. The input material properties utilized for the analysis can be determined based on experimental tests conducted on the braided composite. The correlation between the analysis results and results obtained from quasi-static tensile coupon tests was reasonably good. A representative flat panel test was simulated using the analysis model. The penetration velocity was slightly underpredicted, and the damage patterns obtained were similar to those obtained experimentally. The discrepancy between the experimental and analytical results is most likely due to the effects of strain rate on the material properties which is not currently accounted for within the material model. The analysis model, which utilizes LS-DYNA shell elements, appears promising in its ability to simulate the axial and transverse deformation and failure of the braided material. Future efforts will involve incorporating the effects of strain rate into the model, as well as investigating in more detail the capability of the model to simulate impact events.

References

1. Chou, T.W. and Ishikawa, T.: "Analysis and Modeling of Two-Dimensional Fabric Composites," in Textile Structural Composites, Composite Material Series, vol. 3, T.W. Chou and F.K. Ko, Eds., Elsevier Science Publishers B.V., Amsterdam, 1989, ch. 7, pp. 209–277.
2. Naik, N.K.; and Shembedkar, P.S.: "Elastic Behavior of Woven Fabric Composites: I-Lamina Analysis," Journal of Composite Materials, vol. 26, no. 15, pp. 2196–2225, 1992.
3. Pastore, C.M. and Gowayed, Y.A.: "A Self-Consistent Fabric Geometry Model: Modifications and Application of a Fabric Geometry Model to Predict the Elastic properties of Textile Composites," Journal of Composites Technology and Research, vol. 16, no.1, pp. 32–36, 1994.
4. Byun, J.-H.: "The analytical characterization of 2-D braided textile composites," Composites Science and Technology, vol. 60, no. 5, pp. 705–716, 2000.
5. Tanov, R. and Tabiei, A.: "Computationally Efficient Micromechanical Models for Woven Fabric Composite Elastic Moduli," Journal of Applied Mechanics, vol. 68, no. 4, pp. 553–560, 2001.
6. Bednarcyk, B.A.; and Arnold, S.M.: "Micromechanics-Based Modeling of Woven Polymer Matrix Composites," AIAA Journal, vol. 41, no. 9, 2003.
7. Roberts, G.D et al. "Impact Testing and Analysis of Composites for Aircraft Engine Fan Cases," NASA TM 211493, 2002.
8. Cheng, Jingyun, Material Modeling of Strain Rate Dependent Polymer and 2D Triaxially Braided Composites. Ph.D. Dissertation, University of Akron, Akron, Ohio, 2006.
9. Livermore Software Technology Corporation. LS-DYNA Keyword Manual v 971, Livermore, CA, 2007.
10. Littell, J.D.; Binienda, W.K.; Goldberg, R.K.; and Roberts, G.D.: "A Modeling Technique and Representation of Failure in the Analysis of Triaxial Braided Carbon Fiber Composites," NASA/TM—2008-215245, 2008.
11. Littell, J.D.: "The Experimental and Analytical Characterization of the Macromechanical Response for Triaxial Braided Composite Materials," Ph.D. Dissertation, University of Akron, Akron, Ohio, 2008.
12. Matzenmiller, A.; Lubliner, J.; and Taylor, R.L.: "A Constitutive Model for Anisotropic Damage in Fiber-Composites," Mechanics of Materials 20, 125–152, 1995.
13. Sun, C.T.; and Chen, J.-L.: "A Micromechanical Model for Plastic Behavior of Fibrous Composites," Composites Science and Technology, vol. 40, pp. 115–129, 1991.

14. Li, X.; Binienda, W.K.; and Goldberg, R.K.: “Finite Element Model for Failure Study of Two-Dimensional Triaxially Braided Composite,” NASA/TM—2010-216372, 2010.
15. Daniel, I.M.; and Ishai, O.: Engineering Mechanics of Composite Materials, Second Edition, Oxford University Press, New York, 2006.
16. Pereira, J.M.; Roberts, G.D.; Ruggeri, C.R.; Gilat, A.; and Matrka, T., “Experimental Techniques for Evaluating the Effects of Aging on Impact and High Strain Rate Properties of Triaxial Braided Composite Materials,” NASA/TM—2010-216763, 2010.

REPORT DOCUMENTATION PAGE		Form Approved OMB No. 0704-0188

1. REPORT DATE *(DD-MM-YYYY)*	2. REPORT TYPE	3. DATES COVERED *(From - To)*
01-12-2010	Technical Memorandum	

4. TITLE AND SUBTITLE
Modification of a Macromechanical Finite-Element Based Model for Impact Analysis of Triaxially-Braided Composites

5a. CONTRACT NUMBER

5b. GRANT NUMBER

5c. PROGRAM ELEMENT NUMBER

6. AUTHOR(S)
Goldberg, Robert, K.; Blinzler, Brina, J.; Binienda, Wieslaw, K.

5d. PROJECT NUMBER

5e. TASK NUMBER

5f. WORK UNIT NUMBER
WBS 698259.02.07.03.03.01

7. PERFORMING ORGANIZATION NAME(S) AND ADDRESS(ES)
National Aeronautics and Space Administration
John H. Glenn Research Center at Lewis Field
Cleveland, Ohio 44135-3191

8. PERFORMING ORGANIZATION REPORT NUMBER
E-17498

9. SPONSORING/MONITORING AGENCY NAME(S) AND ADDRESS(ES)
National Aeronautics and Space Administration
Washington, DC 20546-0001

10. SPONSORING/MONITOR'S ACRONYM(S)
NASA

11. SPONSORING/MONITORING REPORT NUMBER
NASA/TM-2010-216922

12. DISTRIBUTION/AVAILABILITY STATEMENT
Unclassified-Unlimited
Subject Categories: 24 and 39
Available electronically at http://gltrs.grc.nasa.gov
This publication is available from the NASA Center for AeroSpace Information, 443-757-5802

13. SUPPLEMENTARY NOTES

14. ABSTRACT
A macro level finite element-based model has been developed to simulate the mechanical and impact response of triaxially-braided polymer matrix composites. In the analytical model, the triaxial braid architecture is simulated by using four parallel shell elements, each of which is modeled as a laminated composite. For the current analytical approach, each shell element is considered to be a smeared homogeneous material. The commercial transient dynamic finite element code LS-DYNA is used to conduct the simulations, and a continuum damage mechanics model internal to LS-DYNA is used as the material constitutive model. The constitutive model requires stiffness and strength properties of an equivalent unidirectional composite. Simplified micromechanics methods are used to determine the equivalent stiffness properties, and results from coupon level tests on the braided composite are utilized to back out the required strength properties. Simulations of quasi-static coupon tests of several representative braided composite are conducted to demonstrate the correlation of the model. Impact simulations of a represented braided composites are conducted to demonstrate the capability of the model to predict the penetration velocity and damage patterns obtained experimentally.

15. SUBJECT TERMS
Polymer matrix composites; Braided composites; Finite element method; Micromechanics

16. SECURITY CLASSIFICATION OF:			17. LIMITATION OF ABSTRACT	18. NUMBER OF PAGES	19a. NAME OF RESPONSIBLE PERSON
a. REPORT	b. ABSTRACT	c. THIS PAGE			STI Help Desk (email:help@sti.nasa.gov)
U	U	U	UU	27	19b. TELEPHONE NUMBER *(include area code)* 443-757-5802